RSC Mechanochemistry

ROYAL SOCIETY OF CHEMISTRY

PAPER

View Article Online
View Journal | View Issue

Cite this: *RSC Mechanochem.*, 2026, **3**, 378

Mechanochemical approach to gallate bioMOFs: efficient synthesis and Cr(VI) removal from aqueous and soil systems

Alisson Luiz Rocha Balbino, †[a] Giovanna Pereira Correia, †[a] Gustavo Henrique Correia dos Santos, [a] Priscilla Jussiane Zambiazi, [a] João Paulo da Silva Souza, [a] Bryan Alberto Laura Larico, [a] Denise de Lima Dias Delarica, [b] Kathleen Fernandes, [b] Mara Regina Moitinho, [b] Luciana Pires Rodrigues Betioli, [b] José Marques Junior, [b] Dagoberto de Oliveira da Silva, [c] Paulo Filho Marques de Oliveira [a] and Liane Marcia Rossi *[a]

Heavy metal atoms, such as chromium, lead, cadmium, and others, are harmful to health and the environment and can cause irreversible impacts at certain concentrations. Given the hazards and increasing levels of chromium in aquatic and soils systems due to anthropogenic activities, it is important to implement heavy metal adsorption technologies for sustainable and green development. Here, two bioMOFs were synthetized *via* mechanochemistry, a solvent-free and environmentally friendly method that enables faster reactions compared to conventional solvothermal synthesis. Both MOFs use gallate as the organic linker, and the reactions were performed using a vibratory ball mill. The Fe-gallate MOF was obtained after 15 minutes of milling and the Mg-gallate MOF, after 60 minutes of milling, both significantly faster than what was reported before. The maximum Cr(VI) removal efficiency (29%) was obtained with the mechanochemically synthesized Fe-gallate. The material was further applied to Cr-rich soil samples, confirming its efficiency in chromium removal from complex matrices. These findings reinforce the potential of mechanochemistry as a sustainable route for the synthesis of advanced materials, particularly bioMOFs, providing greener alternatives from material selection to synthesis and application.

Received 5th October 2025
Accepted 3rd February 2026

DOI: 10.1039/d5mr00123d

rsc.li/RSCMechanochem

1. Introduction

Metal–Organic Frameworks (MOFs) belong to the class of coordination polymers, exhibiting specific structures and functions. Their crystalline networks are constructed through symmetrically directed and oriented topology design. This class of materials possesses a unique identity due to the adjustability of crystallographic pore connectivity and high surface area, which confer intrinsic properties to the material. MOFs are composed of building blocks consisting of metal clusters coordinated to organic ligands, resulting in three-dimensional, two-dimensional, or even one-dimensional networks.[1] Among the various subclasses of MOFs,[2] bioMOFs are distinguished by incorporating renewable and non-toxic organic ligands, such as biomass-derived organic acids (*e.g.* formic, lactic, citric, oxalic). These biomass-derived ligands not only offer promising intrinsic properties such as conformational flexibility, porosity, and coordination diversity, but also have many functional groups that enable a multitude of coordination modes with metal ions and clusters, resulting in exceptional structural diversity ranging from rigid crystalline structures to dynamic MOFs.[3] BioMOFs have demonstrated great potential for various environmental applications, especially in purification and remediation processes in aquatic and soils systems. These materials display essential properties for sustainable environmental technologies, including high adsorption capacity and selectivity under humid conditions, recyclability, cost-effectiveness, durability, and eco-friendly composition.[4–6]

MOFs are promising materials for the removal of chemical contaminants[7] due to their unique and functional properties. The presence of functional groups such as carboxyl, hydroxyl, amine, and thiol provides strong affinity for toxic ions like CrO_4^{2-}, Pb^{2+}, Cd^{2+}, and Hg^{2+}.[8] Among these, gallate-based bioMOFs stand out as a highly effective class, leveraging their porous frameworks and selective binding capabilities.[9] These

[a]*Departamento de Química Fundamental, Instituto de Química, Universidade de São Paulo, Av. Prof. Lineu Prestes 748, São Paulo, 05508-000, Brazil. E-mail: lrossi@iq.usp.br*

[b]*School of Agricultural and Veterinary Sciences, São Paulo State University (FCAV-UNESP), Via de Acesso Prof. Paulo Donato Castellane, s/n, Jaboticabal, São Paulo, Brazil*

[c]*MOF TECH Pesquisa & Desenvolvimento Ltda., Rua Ângelo Mestriner, 263, Ribeirão Preto, São Paulo, 14030-090, Brazil*

† These authors contributed equally to this work.

materials are constructed from gallate ligands derived from gallic acid, a naturally abundant and cost-effective organic compound that occurs in free form or as derivatives in a variety of food sources, such as fruits, vegetables, and beverages, as well as in nuts, tea, grapes, gallnuts, and oak bark. Industrially, gallic acid is mainly obtained through the hydrolysis of tannic acid by tannase.[10–12]. When coordinated to metal centres, gallate ligands form robust metal–organic frameworks, where their strong chelating ability promotes structural stability while the presence of multiple hydroxyl groups enhances interactions with target pollutants[9] In the context of Cr remediation, especially Cr(VI), which is highly toxic, soluble, and mobile in the environment, MOFs have stood out for their ability to operate through different mechanisms.[13–15] MOFs also demonstrate outstanding performance as adsorbents. Certain types are specifically engineered to capture Cr(VI) ions through electrostatic interactions, particularly under acidic pH conditions, where hexavalent chromium predominantly exists as anionic species such as $[CrO_4]^{2-}$ and $[Cr_2O_7]^{2-}$. Following adsorption, chromium can be retained within the MOF pores or precipitated as hydroxides, thereby promoting its immobilization and preventing both groundwater contamination and plant uptake.[15]

High concentrations of Cr in forest soils can occur through various mechanisms, even in environments considered natural or minimally impacted by human activity. One of the main causes is the geological origin of the soil, particularly in areas formed by ultramafic rocks or serpentinites, which are naturally rich in minerals such as chromite ($FeCr_2O_4$) and release Cr during the weathering process. Additionally, atmospheric deposition of contaminated particles from industrial activities, biomass burning, or vehicle emissions can contribute to Cr accumulation in native vegetation areas, especially when these are located near urban centers or industrial zones.[16] These processes highlight the critical need for adopting mitigation strategies to reduce Cr concentrations in such environments, aiming to prevent ecological risks and preserve soil and water quality.[17]

Gallate-based MOFs have been reported with various metal centres, including Fe, Mn, Co, and Ni,[18] Mg,[6,19] Cu,[20,21] and Al.[22] These gallate-based MOFs have shown promise in a wide range of applications, including pollutant removal and catalysis,[9] heterogeneous catalysis and magnetic materials,[18] gas storage—particularly hydrogen—and selective gas adsorption,[6,19] wastewater treatment through dye removal,[21] antioxidant and antimicrobial activity for biomedical and environmental purposes,[20] alongside applications in natural gas separation and purification.[22] These diverse functionalities highlight the versatility of gallate ligands in designing environmentally relevant and functionally robust MOF structures. However, despite their potential, achieving sustainable and scalable syntheses remains a challenge, as MOFs are frequently assessed based on their environmental applications rather than on the sustainability of their production methods.[23]

Mechanochemistry has emerged as one of the most promising approaches for MOF synthesis.[24–26] Since 2006,[27] hundreds of structures have been reported using mechanochemical approaches, which is characterized by the use of solid reactants, the absence or minimal use of solvents, significantly shorter reaction times, and the ability to access novel frameworks.[28] Mechanochemical routes, specially mechanical milling, enable the formation of phases or structures that are difficult—or even impossible—to obtain through conventional synthetic routes.[29] Besides, the synthesis conditions play a critical role in controlling the morphology of the resulting materials.[24] This study explores the mechanochemical ball-milling synthesis of two gallate-based bioMOFs employing abundant and low-toxicity Fe and Mg metal centres, hereafter referred to as Fe-gallate and Mg-gallate, respectively, as well as their potential for Cr removal from aqueous solutions and soil matrices. Although these materials have previously been obtained *via* solvothermal methods, mechanochemical synthesis, as far as we know, was not explored yet. It offers a greener alternative by significantly reducing or eliminating solvent use, shortening reaction times, accessing specific morphologies of materials, and enhancing the sustainability of the production process.

2. Materials and methods

2.1 Materials

The syntheses were performed using iron(II) chloride tetrahydrate ($FeCl_2 \cdot 4H_2O$ 99%), magnesium sulphate heptahydrate ($MgSO_4 \cdot 7H_2O$ 99%), gallic acid monohydrate ($C_6H_2(OH)_3COOH \cdot H_2O$ 99%) and sodium hydroxide (NaOH 90%). The adsorption experiments were performed using potassium chromate (K_2CrO_4 99%) as Cr(VI) source. All chemicals were purchased from Merck.

2.2 Synthesis

2.2.1 Mechanochemical synthesis of Fe-gallate MOF – $Fe(C_7H_3O_4)\cdot 3(H_2O)$. 400 mg (2.0 mmol) of $FeCl_2 \cdot 4H_2O$ was mixed with 720 mg of $C_6H_2(OH)_3COOH$ (4.0 mmol) and 240 mg of NaOH (6.0 mmol) in a 10 mL stainless steel jar with one stainless steel ball ($\varnothing = 10$ mm and 4 g). The reaction was carried out using a Retsch® MM400 vibratory ball mill at 30 Hz during 15, 30, 60 and 90 min. After the mechanochemical synthesis, the resulting powder was washed four times with deionized water and one time with ethanol, then collected by filtration each time. The final product was left to dry in an oven overnight at a 70 °C. The isolated yields obtained after 15, 30, 60, and 90 minutes of milling were 63.5%, 69.1%, 91.6% and 92.3% respectively.

2.2.2 Mechanochemical synthesis of Mg-gallate MOF – $Mg(C_7H_5O_4)\cdot 3(H_2O)$. 460 mg (1.8 mmol) of $MgSO_4 \cdot 7H_2O$ was mixed with 670 mg of $C_6H_2(OH)_3COOH$ (3.7 mmol) and 220 mg of NaOH (5.5 mmol) in a 10 mL stainless steel jar with one stainless steel ball ($\varnothing = 10$ mm and 4 g). The reaction was carried out using a Retsch® MM400 vibratory ball mill at 30 Hz during 15, 30, 60 and 90 min. The same procedure as before was used to collect and dry the samples. The isolated yields obtained after 15, 30, 60, and 90 minutes of milling were 10.9%, 55.7%, 67.7% and 75.2% respectively.

2.3 Characterization

Fe-gallate and Mg-gallate MOFs were characterized using various analytical techniques. Powder X-ray diffraction (XRD)

patterns acquisition was performed using a Shimadzu XRD-7000 X-ray diffractometer at 40 kV and 25 mA operating in reflection mode with Cu-Kα radiation source (λ Cu Kα = 1.5418 Å) in a Bragg–Brentano geometry. Diffraction patterns were recorded in the 2θ range from 5 to 70° with a step of 0.02° and a scanning rate of 2° min^{-1} with an acquisition time of 0.6 s per step (total scanning time of 50 min). A flexible divergence slit and automatic beam height adjustment were employed to maintain a constant irradiated area on the sample surface and suppress unwanted background contributions. LeBail refinement of the PXRD data was performed using the FullProf program. Initial LeBail refinements were performed to obtain an accurate description of the background points with refinable heights, and the peak profiles were described using the Thompson–Cox–Hastings pseudo-Voigt model. The refined background, cell constants, and profile parameters were subsequently transferred to the LeBail refinement step. The refinement employed initial structural models derived from the corresponding single-crystal X-ray diffraction structures for Fe-Gallate and Mg-Gallate obtained from CIF files retrieved from the CCDC crystal structure database. The degree of crystallinity was quantified from the PXRD patterns by separating the contributions of the crystalline and amorphous fractions. The experimental diffractograms were background-corrected and decomposed into sharp Bragg peaks, associated with the crystalline percentage (%) was then calculated as the ratio between the integrated area of the crystalline contribution and the total scattered area (crystalline + amorphous) over the selected 2θ range, as commonly applied in X-ray diffraction analyses of semi-crystalline materials. Fourier transform infrared spectroscopy (FTIR) was conducted with a Shimadzu IR PRESTIGE-21 spectrometer, operating in attenuated total reflectance (ATR) mode. Raman spectroscopy was carried out using a Renishaw inVia micro-Raman instrument, operating with 785 nm laser for Fe-gallate MOF and 633 nm laser for Mg-gallate MOF. The data was collected with a 50× or 100× objective and a 1200 L mm^{-1} grating. Thermogravimetric analysis (TGA) was performed using a TA500 instrument, starting at an initial temperature of 50 °C and increasing up to 900 °C, under a synthetic gas atmosphere, with a heating rate of 10 °C min^{-1}. Scanning electron microscopy (SEM) images were obtained using a field-emission scanning electron microscope JEOL JSM-7401F, after sputter-coating the samples with gold. Surface area measurement was performed using a Quantachrome NOVA-1200e; degassing was carried out at 110 °C for 12 hours, and the area was calculated using the Brunauer–Emmett–Teller (BET) model. XPS spectra were obtained in Scienta Omicron ESCA+ spectrometer equipped with EA-125 analyzer and a Al Kα monochromatic source (1486.6 eV) at a operating pressure of 10–9 Pa. The high-resolution XPS spectra were recorded at 20 eV pass energy using 0.05 eV step and calibrated using adventitious carbon signal at 284.8 eV.

2.4 Cr(VI) adsorption experiment

Firstly, a Cr(VI) solution was prepared by dissolving 194 mg (1.0 mmol) of K_2CrO_4 in 100 mL of deionized water, and then dilution was made as necessary. Besides, all batch experiments were conducted in 15 mL falcon tubes, containing 10 mL of working solution with desired Cr(VI) concentration in contact with 15 mg of desired gallate-MOF.

Time-dependent adsorption of Cr in water was studied with Cr solution of concentration of 100 mg L^{-1} in which samples were taken in periods between 15 min and 40 h. In all experiments, the tubes were placed in an orbital shaker (IKA KS 130 basic) at 640 rpm at room temperature, and the pH measure of 6 was attested before the experiment.

To evaluate the recyclability and reusability of the materials, three cycles of recovery were performed for each MOF, in cycles of 2 h of shaking, followed by centrifugation and drying at 65 ° C. All samples were carried out in solutions with initial concentration of Cr(VI) of 100 mg L^{-1}. After, the samples were washed with 5 mL of solution of HCl 0.01 M, sonicated for 10 min, and then dried at 65 °C. The concentration of Cr(VI) was quantified by inductively coupled plasma optical emission spectrometry, ICP OES (Thermo Scientific, iCAP 7000 series).

The adsorption capacity (q_e) and removal efficiency (R%) are evaluated according to the eqn (1) and (2) described below:

$$q_e = \frac{(C_0 - C_t) \times V}{m} \quad (1)$$

$$R(\%) = \frac{(C_0 - C_t)}{C_0} \times 100 \quad (2)$$

where q_e (mg$_{Cr}$ g$_{MOF}^{-1}$) is the amount of Cr(VI) adsorbed; C_0 (mg L^{-1}) is the concentration of Cr(VI) in the solution before the adsorption; C_t (mg L^{-1}) the concentration of Cr(VI) after adsorption; V (L) is the volume of the experimental solution; and m (g) is the weight of the MOF used.[30]

2.5 Experimental design and evaluation of chromium availability in soils

To evaluate the environmental remediation potential of Fe-gallate MOF in chromium-contaminated soils, an experiment was conducted using soils from three forest areas with varying natural chromium contents (one Typic Hapludult and two Typic Hapludox). Sampling was carried out at georeferenced points, at depths of 0–0.25 m and 0.25–0.50 m, in order to adequately represent the superficial soil profile.

Before the treatments were applied, an initial characterization of Cr concentrations was performed for all samples. Based on these results, the areas were classified as having low, medium, or high Cr content, allowing the establishment of experimental groups with distinct initial conditions. The values presented as "control" in the graphs of Fig. 12 correspond precisely to this baseline, that is, the Cr concentrations determined in the original samples prior to MOF application.

After the treatments were applied, the soil was analysed again following the same analytical protocol used in the initial characterization, ensuring comparability between stages.

Five application rates of Fe-gallate MOF (0, 0.2, 0.5, 1.0, and 4.0 t ha^{-1}) were tested in four replicates. Soil samples (500 g) were incubated in pots and maintained at 50% of their water-

holding capacity for 90 days. Chromium concentrations were determined following USEPA Method 3050B.

The USEPA Method 3050B consists of a strong acid digestion designed to solubilize metals present in the soil matrix. Initially, approximately 1 g of dry soil was transferred to digestion flasks, to which concentrated nitric acid (HNO_3) was added. The mixture was heated to near dryness, with additional portions of HNO_3 added repeatedly until no further brown fumes were released, indicating the oxidation of organic matter. Hydrogen peroxide (H_2O_2) was then added in a controlled manner, followed by additional heating to complete the oxidation of residual organic material. For samples analysed by ICP, the procedure included a reflux step with hydrochloric acid (HCl), which enhances the solubilization of remaining metals. After this step, the digestate was concentrated by heating and subsequently diluted to a final volume of 100 mL with reagent water. The resulting extract was then subjected to instrumental analysis for chromium quantification.

3. Results and discussion

3.1 Reactional system

In most reported syntheses of metal-gallate MOFs, a common strategy involves the use of a strong Lewis base to deprotonate the carboxylic group of gallic acid, thereby facilitating coordination with the selected metal centre. Hydrothermal approaches often involve the dissolution of bases such as NaOH and KOH, in aqueous media to deprotonate the carboxyl groups of gallic acid to promote coordination with metal centres and subsequent framework formation. Alternatively, some solvothermal setups are reported using DMF in water, as in the study reported by Niu H. *et al.*[31] In this system, water at temperatures above 110 °C facilitates the formation of dimethylamine from DMF decomposition and thus promotes the deprotonation of gallic acid. In contrast, our approach adopts the solid-state reaction with NaOH being the strong base. Herein, the synthesis of gallic acid-based MOFs was carried out *via* mechanochemistry using NaOH directly as the base to promote ligand deprotonation, without the need for any additional solvent. Table 1compiles various studies reporting the synthesis of Fe- or Mg-based MOFs derived from gallic acid. When strong bases such as KOH are employed on solvothermal or hydrothermal routes, the reactions are conducted in autoclaves at temperatures above 100 °C and reaction times ranging from 4 to 48 hours. Notably, regarding synthesis time, a recent work[32] reports an alternative route using microwave irradiation to reduce the reaction time to 30 minutes with a water/DMF solvent mixture.

In the mechanochemical synthesis, a milling frequency of 30 Hz was employed to ensure high energy input, while the reaction time was varied from 15 to 90 minutes to identify the minimum duration required for product formation. Stainless steel jars and balls were used as the milling medium, selected for their higher energy transfer efficiency due to the greater density of the alloy.[35] Each jar was loaded with a single steel ball, and approximately 70% of the available volume was filled to optimize milling conditions.

Gallic acid contains three phenolic hydroxyl groups and one carboxylic acid group, all of which can be deprotonated at different pH conditions, allowing the generation of compounds of mixed valances, which can coordinate with metals of charge 2+ or 3+ depending on the extent of deprotonation. The amount of NaOH in the reaction directly impacts which of these groups will be deprotonated and to what extent. The carboxylic group ($pK_a \approx 4.4$) is the most acidic and will be deprotonated first, even with stoichiometric amounts of NaOH. The phenolic hydroxyl groups ($pK_a \approx 8.5$–9.5) require a more basic medium for deprotonation. If the exact stoichiometry for the carboxylic acid group (1 : 1) were used, phenolic hydroxyl groups would remain mostly protonated.

Therefore, a controlled excess of NaOH promotes the deprotonation of one or more phenolic hydroxyl groups in gallic acid, enhancing its ligand reactivity. This modification increases electron density at the coordination sites, ultimately strengthening metal–ligand interactions. A very large excess of base could lead to the complete deprotonation of all three hydroxyl groups, affecting the solubility and reactivity of the resulting anionic species. Thus, in the present work, we decided to use 1.5 times the stoichiometric amount of NaOH, which provides a balance between ensuring complete deprotonation of the carboxyl group and enabling partial deprotonation of the hydroxyl groups, which can be beneficial for the reactivity and coordination of gallic acid in the synthesis of these MOFs. This approach aimed to employ a minimal quantity of base sufficient for the deprotonation of the carboxylate ligands, ensuring controlled reactivity during the synthesis process.[34,36] A ligand-to-metal stoichiometry of 2 : 1 was employed for both Fe- and Mg-based MOFs synthesized with gallic acid. This ratio was selected to match the coordination requirements of the metal centers and the multidentate nature of the ligand, promoting full metal coordination and the formation

Table 1 Comparison of different synthesis conditions for gallic acid-based MOFs, highlighting the solvents used, method and reaction times

Metal	Solvent	Method	Reaction time	Reference
Fe, Mg	Solventless	Mechanochemistry	15–90 min	This work
Fe, Mn, Co, Ni	Water	Microwave	4 hours	18
Ni, Mg, Co	Water	Hydrothermal	24 hours	33
Mg	DMF/water	Microwave	30 min	32
Fe	DMF	Solvothermal	24 hours	31
Fe, Mn, Co, Ni	Water	Solvothermal	72 hours	1
Fe	Water	Hydrothermal	48 hours	34

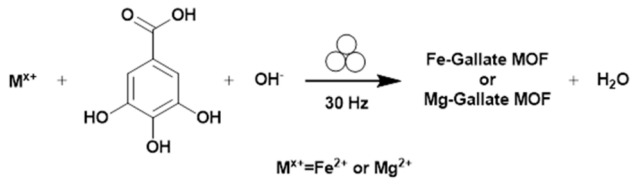

Fig. 1 Mechanochemical synthesis of gallate-based MOFs.

of extended and stable frameworks. In the case of the Fe-based material, the use of a ligand excess also helps to suppress the formation of iron oxide or hydroxide secondary phases under mechanochemical conditions, whereas for the Mg-based system it ensures adequate stabilization of the coordination environment and prevents the formation of poorly crystalline non-framework phases.

The observed yields (for Fe-gallate obtained after 15, 30, 60, and 90 minutes of milling 63.5%, 69.1%, 91.6% and 92.3% respectively; for Mg-gallate obtained after 15, 30, 60, and 90 minutes 10.9%, 55.7%, 67.7% and 75.2% respectively) indicate a strong dependence on milling time. For both Fe- and Mg-based MOFs, shorter reaction times (15 minutes) resulted in significantly lower yields (63.5% and 10.9%). In contrast, extended milling (90 minutes) led to remarkably high yields, particularly for the Fe-based MOF, which reached up to 93%. The consistently lower yields for the Mg-based MOF under identical conditions may reflect differences in the coordination kinetics or reactivity. These findings underscore the importance of reaction time as a critical parameter for optimizing mechanochemical synthesis and suggest that further refinement could identify the optimal balance between yield and energy efficiency. The expected reaction is presented in Fig. 1.

3.2 Characterization of gallate MOF

Fig. 2a and b shows PXRD collected data of Fe-gallate MOF at different milling times, which is consistent with previously reported results.[37] Powder X-ray diffraction patterns reveal that the synthesized MOFs are isostructural, as the experimental profiles match the reference patterns of CCDC 1260549 (Fe-gallate)[37] and 1899504 (Mg-gallate),[19] and the refined unit cell parameters agree with the reported values within experimental uncertainly. The PXRD analysis therefore confirms phase purity and isostructurality but does not constitute a full structural refinement from powder data. For the Fe-gallate, the most intense reflection indexed as (1 0 0) exhibits a systematic shift in 2θ with milling time, which is consistent with small variations in the refined lattice parameters reflection shifts in the opposite direction, indicating a slight lattice contraction. These changes are discussed as indicative of subtle framework distortions rather than a full reorganization of the underlying topology. Although the PXRD data do not allow a direct measurement of pore size from diffraction alone, the combination of the refined cell metrics and adsorption results suggests that Mg-gallate exhibits a higher accessible pore volume and specific surface area than Fe-gallate.

The oxidation state of Fe in the Fe-gallate MOF was evaluated by high-resolution X-ray Photoelectron Spectroscopy (XPS) in the Fe 2p photoemission region (Fig. S3). The Fe $2p_{3/2}$ signal can be deconvoluted into two components located at 711.1 and 714.6 eV, which are assigned to Fe(II) and Fe(III), respectively.[31] Similarly, the Fe $2p_{1/2}$ peak exhibits two components at 725.2 and 729.3 eV, which are also attributed to Fe(II) and Fe(III), respectively.[31] The overlap of the satellite peak at 718.0 eV reveals the predominance of Fe(II) as the oxidation state of Fe in the MOF structure.[49,50] However, the results also indicate that Fe undergoes partial oxidation after MOF formation, likely associated with the exposure of Fe(II) species to an oxidizing atmosphere. Despite this partial oxidation, the surface Fe(III)/Fe(II) ratio, estimated from the relative areas of the fitted components, is approximately 38%, which is slightly lower than the value previously reported for this material.[31]

Considering the absence of significant changes in peak position and patterns obtained for the Fe-gallate MOF after 15

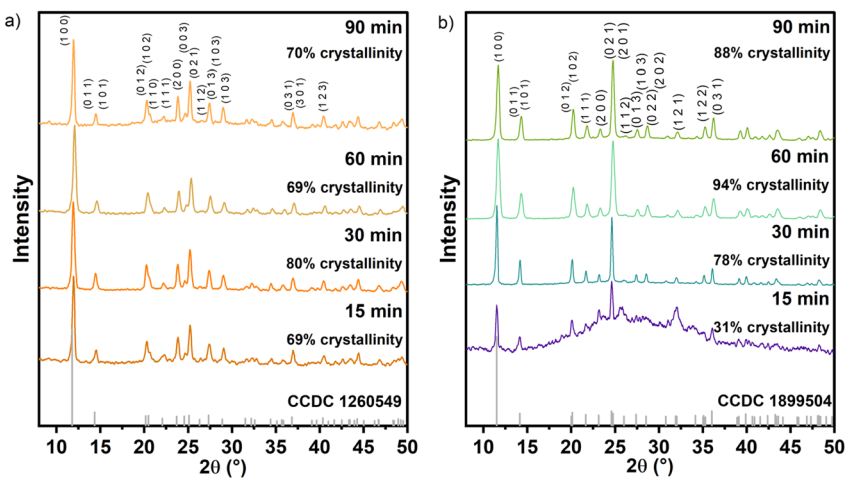

Fig. 2 PXRD standard for M-gallate MOFs, for (a) Fe-gallate and (b) Mg-gallate, prepared *via* mechanochemistry at different reaction times (15, 30, 60, and 90 minutes) and the respective degrees of crystallinity (%) calculated for each PXRD standard, indicating the shift of the main diffraction peaks indicated by the *hkl* reflection indices based on the reference model structures obtained from the CCDC database (CCDC codes: 1260549 for Fe-gallate and 1899504 for Mg-gallate).

minutes of the reaction time. The relative crystallinity as obtained from whole-pattern decomposition reaches a plateau, indicating that this milling time is sufficient to stabilise the crystalline phase (Fig. 2a). In contrast, for Mg-gallate MOF (Fig. 2b), the progressive increase in the integrated intensity of the Bragg peaks relative to the amorphous halo reveals a marked crystallinity gain up to 30 minutes, after which no further significant improvement is observed.

The description of the metal coordination environments, protonation states and pore architecture is based on the reported single-crystal structure deposited under CCDC 1260549 [37] and 1899504,[19] which are used here as structural models for Fe-gallate and Mg-gallate, respectively for the LeBail refinement (Fig. S1, S2 and Table SI3). According to these published structures, the chemical formula associated with each MOF is $Fe(C_7O_5H_3)$ for Fe-gallate and $Mg(C_7O_5H_4)$ for Mg-gallate, both with the frameworks crystallise in the primitive trigonal space group $P3_121$ (no. 152 of I.T of C.), with respectively unit cell parameters $a = b = 8.664$ Å, $c = 10.861$ Å, $\alpha = \beta = 90°$, $\gamma = 120°$ for Fe-gallate and $a = b = 8.867$ Å, $c = 10.772$ Å, $\alpha = \beta = 90°$, $\gamma = 120°$ for Mg-gallate, with one-dimensional interconnected channels along the crystallographic *c*-axis, formed by distorted M–O octahedra linked by gallate ligands. In the molecular structures of M-gallate (Fig. 3a and b), each metal centre is coordinated by four oxygen atoms from phenolic hydroxyl groups and two oxygen atoms from carboxylate groups. This arrangement accounts for four gallate ligands per metal centre in the structure. Furthermore, the Mg-gallate MOF presents two protonated oxygen atoms of the hydroxyl group at the phenyl extreme positions, conferring exposed acidic sites within the internal cavities of the porous structure. This distinction between the Fe-gallate and Mg-gallate MOFs may potentially enhance the adsorption capacity of heavy metals onto the active surface of the MOF containing these acidic sites. In the case of Fe-gallate, the trivalent metal ion maintains charge neutrality within the material, resulting in a more compact crystalline unit cell due to the smaller ionic radius. The higher specific surface area measured for Mg-gallate relative to Fe-gallate is consistent with the larger unit cell volume reported for the Mg analogue and with the presence of protonated hydroxyl groups that generate accessible acid sites within the channels. However, given the limitations of our powder data, these structure–property with correlations should be regarded as qualitative and are discussed in conjunction with sorption and adsorption measurements. Additionally, these sites could catalyse reduction processes of adsorbed species.[38] The crystal structure of the MOFs reveals trigonal-shaped channels, with cavities of approximately 9 Å in size connected by narrower windows of 3.6 Å, as visualized in the *ab* and *ac* crystallographic planes, respectively. The porous cavities present in the crystal structure are initially filled with water molecules (Fig. 3c and d), which can be easily removed, resulting in empty pores.[19]

Fig. 4 compares the specific surface areas (SSA) of the Fe-MOF and Mg-MOF samples. The Fe-MOF exhibited SSAs of 81, 62, and 90 $m^2\ g^{-1}$, whereas the Mg-MOF yielded significantly higher values of 101, 89, and 158 $m^2\ g^{-1}$ for synthesis times of

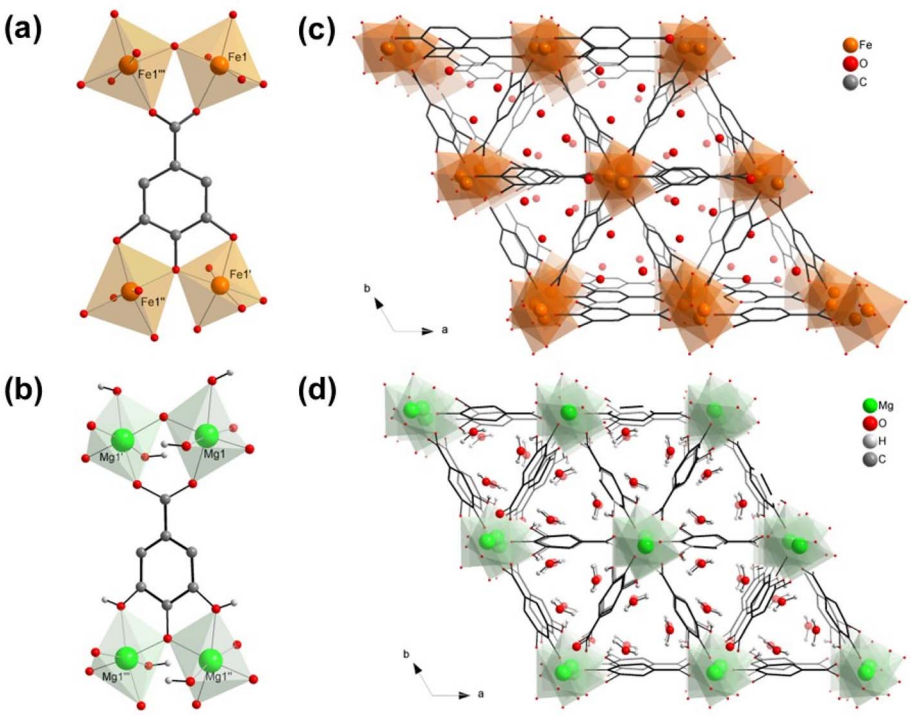

Fig. 3 Projection of molecular structures (a) Fe-gallate and (b) Mg-gallate, highlighting the coordination polyhedra of the Fe and Mg metal centers; and projection of crystal structures (c) Fe-gallate and (d) Mg-gallate, highlighting the frameworks of the MOF structures and the pore spaces filled with water molecules. The crystal structure data was obtained from the CCDC crystal structure database and used as a model reference for LeBail refinement.

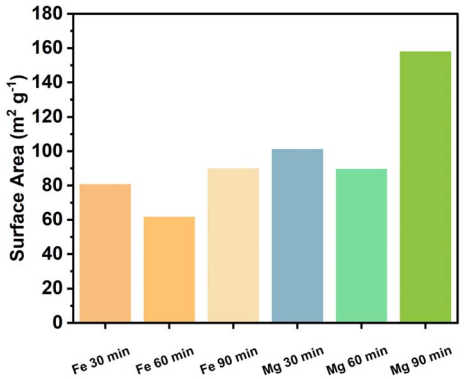

Fig. 4 Surface areas of Fe-gallate MOF and Mg-gallate MOF samples synthesized *via* a mechanochemical route at different times.

30, 60, and 90 min, respectively. This divergence in surface area can be attributed to the distinct chemical nature of the metallic centres, encompassing variations in ionic radius, coordination environments, oxidation states, and the strength of the coordination bonds with the gallate ligand. As observed in Fig. S4, the N_2 adsorption isotherms at low relative pressures exhibit a predominantly type I(b) profile, which is characteristic of materials with relatively broad micropore size distributions. Micropore volumes were determined using the Dubinin–Radushkevich (DR) method, yielding values of 0.029, 0.022, and 0.032 cm^3 g^{-1} for Fe-gallate, and 0.038, 0.032, and 0.057 cm^3 g^{-1} for Mg-gallate at 30, 60, and 90 min of grinding, respectively. These results confirm the superior pore volume of Mg-gallate, demonstrating a direct correlation where the increase in pore volume follows the enhancement of the specific surface area. Mg-gallate is further distinguished by the presence of additional acidic sites, a feature that likely contributes to its higher surface area relative to Fe-gallate.

Synthesis time exerts a direct influence on the surface area through a mechanochemical annealing effect. Since the unit cell of Mg-gallate is larger than that of Fe-gallate, the latter exhibits a more restricted surface area and smaller pores, as supported by the experimental evidence. At 60 min of grinding, the materials reach a state of maximum lattice strain and partial structural disorder, which is reflected in the transient decrease in surface area. By 90 min, however, the accumulated energy from the mechanical impacts triggers an *in situ* annealing process, promoting framework recrystallisation. This structural restoration effectively "clears" previously obstructed channels of defects and amorphous fragments, resulting in the significant spike in the specific surface area of the materials.[39]

An interesting result regarding these materials is related to the morphology of the formed particles. Scanning electron microscopy (SEM) images (Fig. 5) demonstrate that the synthesis duration plays a significant role in the stabilization process of the resulting particles. For the Fe-gallate MOF, roundish particles are observed at all milling times (15, 30, 60, and 90 minutes), indicating a rapid nucleation and growth process. Nevertheless, a reasonable particle size uniformity is only attained after 60 minutes of synthesis, suggesting that this duration is necessary for morphological stabilization. In contrast, for the Mg-gallate MOF, a more uniform particle morphology appears only after 60 minutes of synthesis and persists at 90 minutes. At shorter synthesis times (15 and 30 minutes), the SEM images display particles with clear signs of polydispersity, that is, the presence of particles with visibly different sizes and shapes within the same image. This can be observed in Fig. 5 by the coexistence of larger and irregular particles partially formed at 15 minutes, followed by smaller and irregular particles at 30 minutes. A progressive transition, from irregular non-uniform structures toward more homogeneous and spherical particles is observed as milling time increases, with the initial appearance of spherical particles at 30 minutes, suggesting that extended synthesis time favours the formation of more uniform morphologies. Both Mg- and Fe-gallate MOFs synthesized after 60 minutes exhibit spherical particles, in agreement with previous reports in the literature, where similar morphologies were obtained through careful control of solvent, base, reaction time, and temperature.[31,32] In contrast, when employing a mechanochemical approach, such control parameters are unnecessary, as the reaction occurs by milling solid reagents and external heating is not used. Additionally, SEM images (Fig. 5) revealed the presence of channel-like structures, a feature commonly associated with MOF particle aggregation under conditions of uniform spherical particle distribution.[40] Compared to MOFs synthesized by conventional hydrothermal or solvothermal methods, the materials produced in this study exhibit a similarly homogeneous—or even more organized—morphological distribution. Notably, this structural characteristic is preserved even when mechanochemistry is employed as the synthesis route.[31,32]

The well-defined channels and controlled particle aggregation is particularly relevant for applications in gas adsorption and heavy metal removal. Channel-like structures can enhance the accessibility of active adsorption sites, facilitate molecular diffusion and increase adsorption efficiency. Previous studies have demonstrated that MOFs with hierarchical porosity and interconnected channels exhibit superior performance in gas separation, CO_2 capture, and heavy metal adsorption due to their optimized surface area and transport properties.[41] Additionally, the fact that this morphology was maintained through mechanochemical synthesis highlights the potential for scalable, solvent-free production of bioMOFs with tailored porosity, making them more sustainable for environmental applications.

The chemical environment of the MOFs was studied by FTIR and Raman spectroscopy. The FTIR and Raman spectra (Fig. 6a and b) of Fe-gallate MOF synthesized at 15, 30, 60 and 90 minutes indicate similar patterns. The Raman spectra show asymmetric and symmetric stretching C=O modes of the coordinated COO near 1581 and 1473 cm^{-1}, respectively, which is consistent with the bridging carboxylate functionality associated with the complexation with iron ions.[5] The FTIR spectra show C=C axial deformation in aromatics appeared around 1500 cm^{-1}, in a medium intensity, while the band at 1381 cm^{-1} indicates the O–H deformation and 1236 cm^{-1} the C–O axial deformation.[42,43] The peak revealed at 1078 $cm^{-1}$of Mg-gallate MOF (Fig. 6c) show similar patterns especially for the synthesis at 30, 60 and 90

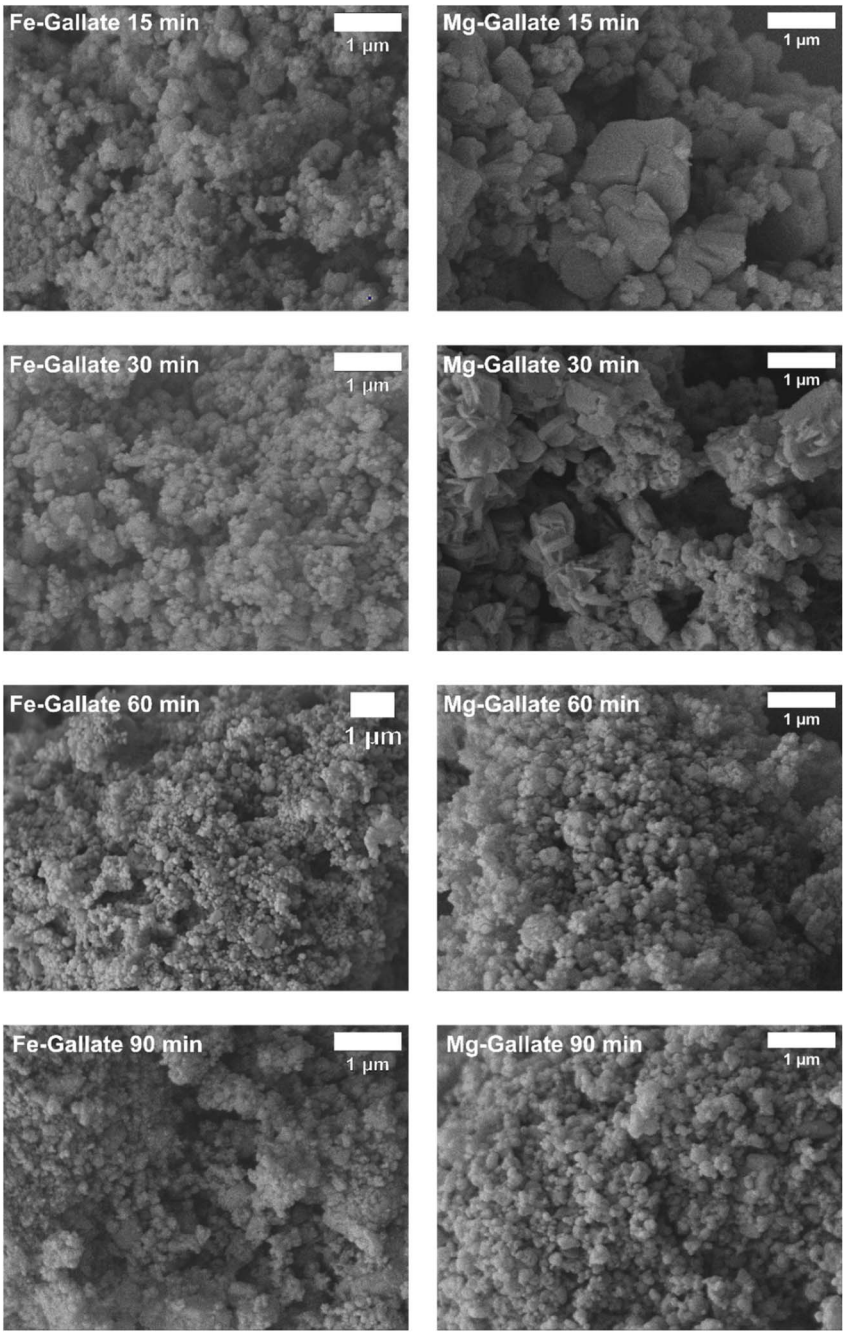

Fig. 5 Scanning electron microscopy images of Mg-gallate and Fe-gallate MOFs mechanochemically synthesized at different times.

minutes. Symmetric and asymmetric stretching modes of the coordinated COO^- are indicated by the peaks in 1610 and 1425 cm^{-1}, respectively, suggesting a deprotonation of the carboxylate group due to the complexation with magnesium ions. In the FTIR spectrum (Fig. 6d) the C=C axial deformation in aromatics signal showed up at 1530 cm^{-1}, while the band at 1441 cm^{-1} indicated the C–O bond. The peak in 1088 cm^{-1} is assigned to the deprotonated carboxyl group, as result of the Mg–O bond formation. For the 15 minute sample, the distortion in both the C=C and $-COO^-$ band suggests a different structure of the material, which is not stabilized at this period of the synthesis.

Thermal stability of the materials was assessed by thermogravimetry (TGA). TGA results (Fig. 7a) of Fe-gallate MOF show three main weight losses, 73 °C and 136 °C are related to surface water and crystallization water loss, respectively, and another in 257 °C related to the thermal decomposition of the gallate ligand. The water content in the structure represents 19.3% of its mass which means a proportion of three molecules of water within the structure of $Fe(C_7O_5H_3)$, which is consistent with the crystalline structure (Fig. 3) and other reports indicate at least two molecules.[33,34,43,44] The ligand degradation begins at 257 °C and reaches its peak at 301 °C.

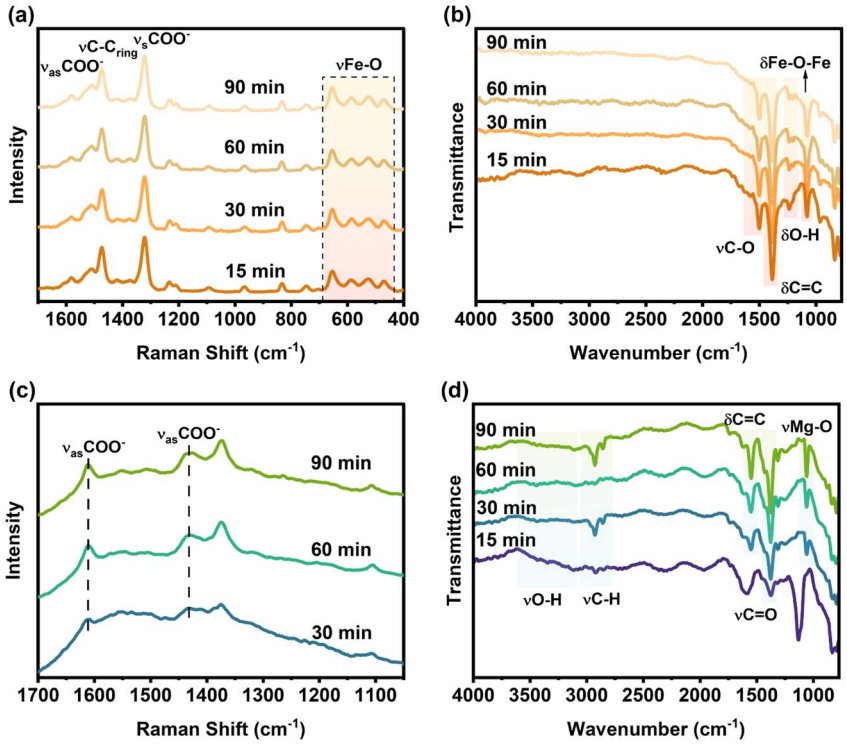

Fig. 6 (a) Raman spectra of Fe-gallate from 1700 to 400 cm^{-1} and (b) FTIR spectra of Fe-gallate MOF samples obtained with different reaction times; and (c) Raman spectra of Mg-gallate from 1700 to 400 cm^{-1} and (d) FTIR spectra of Mg-gallate MOF samples obtained with different reaction times.

PXRD analysis of the residue obtained after the thermal decomposition (Fig. S5) indicates the formation of Fe_2O_3, consistent with hematite (α-Fe_2O_3) phase. Other studies regarding thermal decomposition of ferric compound also indicates hematite as obtaining product in samples calcinated in oxidative atmosphere, with the decomposition occurring mainly in two steps:[45] (I) rapid dehydration following by (II) decomposition to Fe_2O_3. As a result, the pathway degradation can be described as listed below:

$$Fe(C_7O_5H_3)\cdot 3H_2O \rightarrow Fe(C_7O_5H_3) + 3H_2O \text{ (step I)} \quad (3)$$

$$2Fe(C_7O_5H_3) + 12O_2 \rightarrow Fe_2O_3 + 14CO_2 + 3H_2O \text{ (step II)} \quad (4)$$

For the Mg-gallate MOF, the TGA results (Fig. 7b) indicate two weight loss steps, with significant mass losses of 20% and 60%. The DTG curve highlights decomposition events at 30 °C, 151 °C, 223 °C, and a major thermal degradation peak at 466 °C. The structural water content, representing 20% of the mass which also gives 3 molecules of water, which is also consistent with the crystalline structure and other reports for $Mg(C_7O_5H_4)$ structure.[39] The ligand degradation occurs slowly, beginning in 223 °C and reaching its peak at 466 °C. PXRD analysis of the residue obtained after the thermal decomposition (Fig. S5) indicates the formation of MgO. Assuming a similar decomposition pathway with $Fe(C_7O_5H_3)\cdot 3H_2O$, the thermal decomposition of Mg-GA can be described as followed:

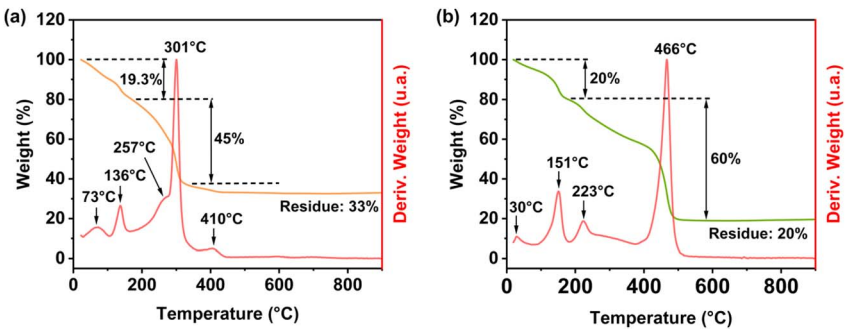

Fig. 7 Thermogravimetric analysis results of (a) Fe-gallate MOF obtained mechanochemically after 60 minutes and (b) Mg-gallate MOF obtained mechanochemically after 60 minutes.

$$Mg(C_7O_5H_4)\cdot 3H_2O \rightarrow Mg(C_7O_5H_4) + 3H_2O \text{ (step I)} \quad (5)$$

$$Mg(C_7O_5H_4) + 6O_2 \rightarrow MgO + 7CO_2 + 2H_2O \text{ (step II)} \quad (6)$$

3.3 Cr adsorption

The first gallic acid-based MOFs applied for environmental water remediation was reported by Niu H. *et al.* (2017),[31] who synthesized a one-dimensional (1D) iron-gallate MOF and evaluated its performance for Cr(VI) adsorption in aqueous solutions with initial Cr(VI) concentrations ranging from 100 to 2000 mg L^{-1}, as well as in electroplating wastewater samples. Although the application of 1 g L^{-1} of the 1D iron-gallate MOF resulted in high removal efficiencies (82–97%) for synthetic Cr(VI) solutions within this concentration range, treatment of real electroplating effluents required optimization of the adsorbent dosage. In this case, dosages between 2 and 10 g L^{-1} led to removal efficiencies ranging from 15.9 to 52.6%.[31] In another study of water remediation, Azhar *et al.* (2020) reported the use of a copper-gallate MOF for the removal of organic dyes, such as methylene blue (MB) and Congo red (CR), achieving removal efficiencies of 65–95% and 55–94%, respectively, with a strong dependence on solution pH.[21] In both studies, the gallate-based MOFs were synthesized using solvothermal or microwave-assisted approaches, employing DMF as the solvent and requiring elevated temperatures (90–120 °C) and extended reaction times ranging from several hours up to 24 h.

In this context, based on the characterization of Fe-gallate and Mg-gallate MOFs synthesized *via* a mechanochemical route using 15 to 90 min milling process, the Cr(VI) adsorption performance of both MOFs was evaluated during 40 h of experiment, with the samples obtained in a 60 min milling process, as shown in Fig. 8. When compared with previously reported solvothermal and microwave-assisted gallate MOFs, the mechanochemically synthesized materials are obtained under significantly milder and more environmentally benign conditions and eliminate the use of toxic organic solvents.

The experiments were conducted to monitor the time-dependent adsorption of Cr(VI) on Fe-gallate MOF at an initial Cr concentration of 100 mg L^{-1} (Fig. 8), and adsorption kinetic models were analysed to investigate how similar the materials would perform. Four kinetic models were examined, including pseudo-first-order, pseudo-second-order, intra-particle diffusion model and Elovich and the correlation coefficient were compared (Table SI4).

For the Fe-gallate MOF, the results displayed in Fig. 8a indicates that the Cr adsorption seems to occur rapidly in the initial stages, and evolves after 8 hours in progressive deceleration of adsorption, reaching a maximum removal efficiency around 24 hours, and stabilizing after, with a adsorption

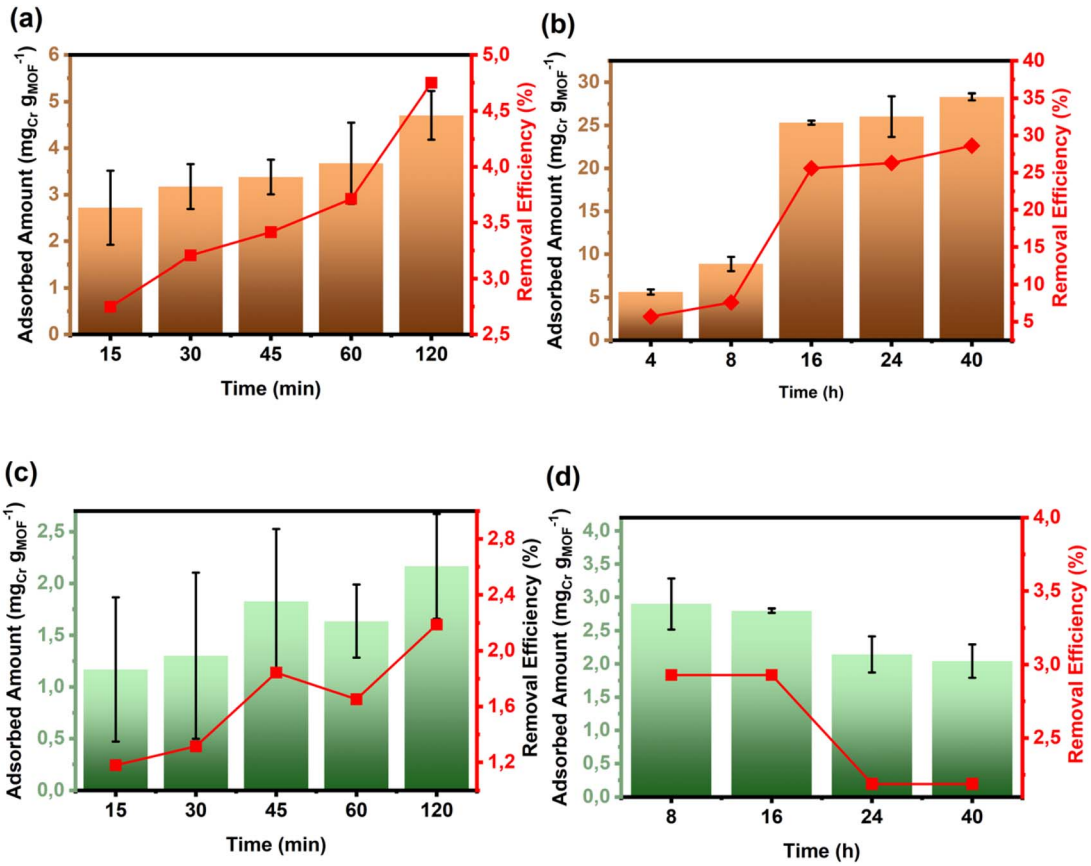

Fig. 8 Adsorption of Cr results using Fe-gallate and Mg-gallate MOF obtained after 60 minutes of milling (a and b) Fe-gallate MOF temporal evolution of adsorption process (from 15 min to 40 h of experiment) using a 100 mg L^{-1} as initial Cr concentration, (c and d) Mg-gallate MOF temporal evolution of adsorption process (from 15 min to 40 h of experiment) using a 100 mg L^{-1} as initial Cr concentration.

capacity of 28 mg_{Cr} g_{MOF}^{-1}. Thus, the optimal adsorption time for Cr removal using Fe-gallate MOF is determined to be between 8 and 24 hours.

Investigating the kinetic models for Cr(VI) adsorption in Fe-gallate, both pseudo-second order and Elovich model displayed the highest values with R^2 of 0.99, while the intra-particle diffusion model displayed the lowest, with R^2 of 0.98 and the pseudo-first order with R^2 of 0.94 (Fig. S6). Both pseudo-second order and Elovich model indicate the predominance of chemical adsorption, where Elovich model also suggests heterogeneous active sites on the surface and within the material, that can limit the adsorption process.[46] Both models fit well with the experimental data, especially the Elovich model suggest that the progressive deceleration of adsorption is caused by the morphology characteristic of the material.

Given the crystalline structure and the surface area of the Fe-gallate, it is also possible a correlation between the removal efficiency and the surface area, being 62 m^2 g^{-1}, meaning while the adsorption of the Cr occurred, a rapid saturation of the available sites of the surface also occurred.

The PXRD and SEM images (Fig. 9) of the Fe-gallate samples after adsorption in a Cr(VI) solution with a concentration of 100 mg L^{-1} indicate that the duration of the experiment affects, to some extent, the crystallinity and morphology of the material. Prior to adsorption, the SEM images show predominantly roundish particles. This general morphology is preserved after the adsorption process, however, signs of particle coarsening and aggregation can be observed, evidenced by the partial coalescence of adjacent particles.

Although these results are promising, the removal efficiencies are still lower than those reported for conventionally synthesized Fe-gallate MOFs *via* the solvothermal method. Niu H. *et al.* (2017)[31] reported the adsorption of Cr(VI) by 1D iron-gallate MOFs, achieving ranges of 82 to 90% removal efficiency, which is higher than that obtained in the present study (29%). This difference may be attributed to variations in morphological properties induced by mechanochemical synthesis. Nevertheless, the mechanochemical approach offers notable advantages, including significantly shorter preparation time and solvent-free synthesis.

For the Mg-gallate MOF, Fig. 8c displays the adsorption kinetics using an initial concentration of 100 mg L^{-1}. The MOF exhibits a rapidly adsorption in the initial stages until 8 hours, however with an adsorption capacity lower than Fe-gallate MOF, with values between 1.2 and 3.0 mg_{Cr} g_{MOF}^{-1}. Within 8 to 16 hours there is a stability of adsorption, reaching a maximum removal efficiency, and after evolves in an abruptly decreasing ratio of adsorption, which suggests Cr releasing in the system, probably due to degradation of the material, an indication of limitation. Investigating the kinetic models for adsorption, the pseudo-second-order, Elovich and intra-particle diffusion model shows the highest correlation, all with $R^2 = 0.97$, while pseudo-first order model gave the lower correlations, with R^2 of 0.80 (Fig. S6). The pseudo-second order confirms the predominance of chemical adsorption, in which Elovich model suggests that as the adsorption occurs, heterogeneous sites are created, probably through the presence of acidic sites within the crystalline structure of Mg-gallate MOF, which is not present for Fe-gallate MOF. The acidic sites can facilitate the adsorption both on the surface and on the porous structure of the material, however, it is possible to favor the degradation as the interaction occurs, contributing to a lower removal efficiency of Cr.

The PXRD and SEM images (Fig. 10) of the Mg-gallate samples after the adsorption in a Cr solution with a concentration of 100 mg L^{-1} reveal significant crystallinity and morphological changes, which are more pronounced than those observed for Fe-gallate, especially in the morphology. These alterations suggest that chemical reactions occurred at the material surface during the adsorption process, likely involving acidic sites within the crystalline structure. This observation further indicates that such sites may play an important role in the chemical stability of the MOF under strongly oxidizing and acidic conditions.

To investigate the chemical changes in the MOFs induced by the adsorption process, XPS spectra were collected for both materials before and after Cr adsorption (Fig. S7 and S8). In the Cr 2p photoemission region, a pronounced contribution from Cr(III) species is observed after use, along with a smaller fraction assigned to Cr(VI). This result suggests that partial reduction of Cr(VI) may occur during the adsorption process. However, further investigations are required to determine whether this reduction takes place at the adsorption sites of the material or if Cr(III) species are released into the solution.

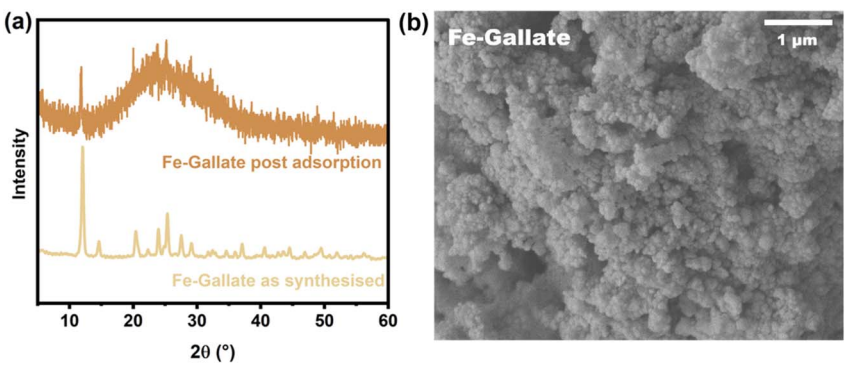

Fig. 9 (a) PXRD pattern and (b) scanning electron microscopy images of Fe-gallate MOF after Cr adsorption.

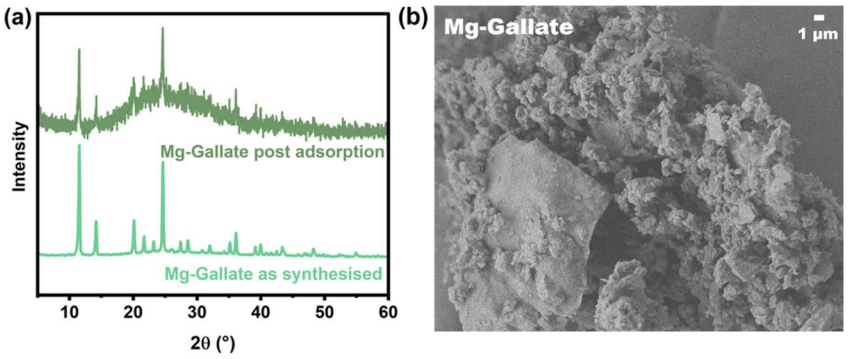

Fig. 10 (a) PXRD pattern and (b) scanning electron microscopy images of Mg-gallate MOF after Cr adsorption.

In the C 1s photoemission region, four components are observed: at 284.8, 286.4, 288.6, and 290.7 eV, referring to adventitious carbon, C–OH of gallate, COO^{-}, and $\pi \rightarrow \pi^{*}$ shakeup peak[34] (Fig. S7). No changes are observed after the Cr adsorption experiment, except for a decrease in the intensity of the peak at 288.6 eV, which can be attributed to the protonation of the carboxylate. Similar changes are observed in the case of Mg-gallate MOF (Fig. S8). In the O 1s region, only two signals are observed at 531.8 and 533.4 eV, attributed to the carboxylate oxygen atoms bonded to the Fe atom in the MOF and Fe–OH, respectively[34] (Fig. S7). Although they do not undergo appreciable shifts after the use of MOF, two new peaks appear at 534.3 and 530.3 eV, which are attributed to adsorbed water and oxygen atoms bound to Cr, respectively. This evidence shows an appreciable interaction between the MOF surface and ion chromate. The same effect is observed in the case of Mg-gallate MOF (Fig. S8). After using MOF, two peaks appear referring to Cr 2p photoemissions (Fig. S7). The peaks can be deconvoluted into two components, forming four components centred at 577.4 and 587.2 eV, attributed to the Cr $2p_{3/2}$ and Cr $2p_{1/2}$ signals of Cr(III) species, respectively, and two components at 579.5 and 590 eV, referring to Cr(VI). The observation of Cr(III) signals indicates that there is a Cr(VI) reduction process, which is in line with what has been observed in experiments on the adsorption and removal of Cr in solution reported in the literature.[31] This phenomenon also occurs when Mg-gallate MOF is applied (Fig. S8).

The recyclability of both Fe-gallate and Mg-gallate MOF is shown in Fig. 11. For the Fe-gallate MOF, the results indicate a stability during the first two cycles, followed by a significant drop in the third cycle, with values of adsorption capacity declining from 15 to 10 $mg_{Cr}\ g_{MOF}^{-1}$, while the Mg-gallate presents a significant drop from second cycle, with values of adsorption capacity varying 6.2 to 4.9 to 5.6 $mg_{Cr}\ g_{MOF}^{-1}$ in each cycle.

The washing solutions of the samples were analysed to investigate the metal leaching of the materials after the adsorption experiments. The results indicate a ratio of Cr recuperation of 6.2 to 8.8% and 1.7 to 3.2% for Fe-gallate and Mg-gallate, respectively, after the cycles. Although small, the values indicate different strength of interactions between Cr with each of the materials, in which the higher Cr recuperation for Fe-gallate suggest a stronger interaction in comparison with Mg-gallate MOF. Raman spectra after the washing procedures (Fig. S9) indicates a remaining of Cr, which is linked with stretches in the region of 532 and 558 cm^{-1} for Fe-gallate and Mg-gallate respectively, attributed to $\nu_{Cr-O-Cr}$.[47,48] For Fe-gallate, this stretch is displayed in the same region of ν_{Fe-O}, in a medium intensity, what can explain the stronger interaction than for Mg-gallate, that has a weaker single band.

Both MOFs are susceptible to metal centre leaching during the cycles, with values of 15 to 17% for Fe and 22 to 29% for Mg. Specially for Mg-gallate MOF, the higher values prejudicated the most its performance, mainly its reusability, once the material

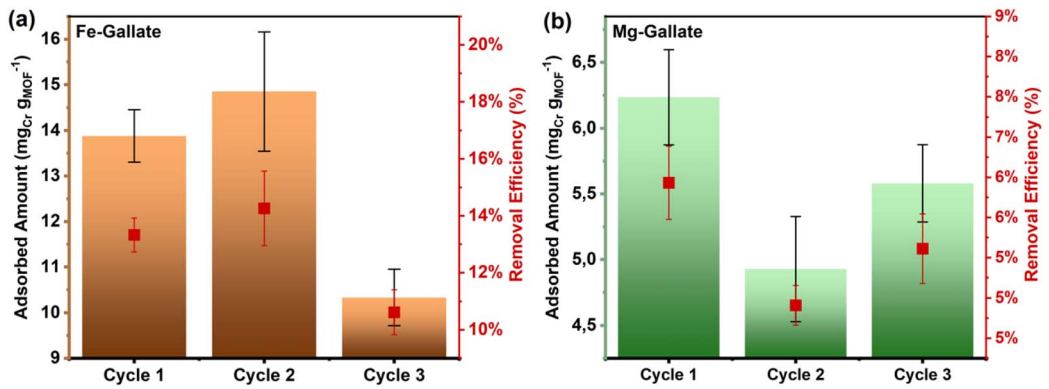

Fig. 11 Adsorption of Cr results using Fe-gallate (a) and Mg-gallate MOF (b) obtained after three cycles.

degradation limited the adsorption capacity and invalidated the analysis after the first cycle of adsorption.

Although the application of both gallate-based MOFs for Cr(VI) removal has shown promising results, further studies are needed to better understand the physicochemical aspects involved in this process. In-depth investigations, including adsorption modelling, as well as kinetic and thermodynamic studies, are essential to elucidate the interaction mechanisms between the material and the contaminant and to assess the actual potential of these MOFs in practical environmental remediation scenarios or even for more fundamental studies. However, above all, the synthesis of MOFs without the use of solvents and with significantly reduced reaction times highlights the efficiency of mechanochemistry as a method for producing bioMOFs.

3.4 Effect of Fe-gallate MOF application on Cr removal from forest soils

The application of different doses of Fe-gallate MOF influenced Cr concentrations in forest soils are shown in Fig. 12.

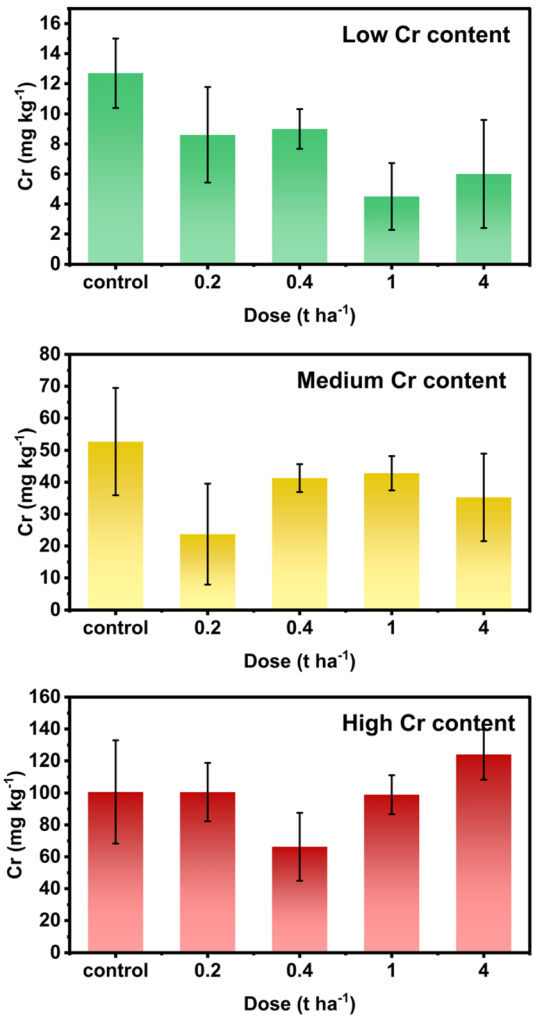

Fig. 12 Means and respective standard error bars, for low, medium, and high Cr levels in forest soils, as influenced by treatments with different MOF doses (0.2, 0.5, 1, and 4 t ha^{-1}) and the control (no MOF application).

Overall, a decreasing trend in Cr concentrations was observed with the application rate, and this trend was more pronounced in soils with medium and low initial Cr levels. In the soil with low Cr content, the application rate of 1 t ha^{-1} was the most effective, reducing Cr levels from 12.7 mg kg^{-1} (control) to 4.5 mg kg^{-1}, a reduction of approximately 65%. In the soil with medium Cr content, the application rate of 0.2 t ha^{-1} resulted in a 42% decrease, from 40.6 mg kg^{-1} (control) to 23.7 mg kg^{-1}. However, Fe-gallate MOF application had little effect for the high Cr content soil, with concentrations remaining between 100 and 120 mg kg^{-1} across all treatments. The overlapping error bars suggest that the reductions were not statistically significant, which may be attributed to rapid saturation of material adsorption capacity in the presence of high Cr concentrations, which is consistent with the aqueous tests performed. These results highlight the potential of MOF as a strategy for mitigating Cr concentrations in soils, particularly in environments with moderate to low initial levels of the element.

Regarding the structural integrity of the MOF during the treatment, we do not have evidence that the material remains intact after its application to the soil. The environmental conditions of the soil, particularly in the soils analyzed in this study, favor the mineralization of the MOF's organic framework. Our working hypothesis is that an isomorphic substitution occurs between the components released from the MOF and the soil mineral matrix, which would explain the reduction observed in Cr concentrations after the treatment.

4. Conclusions

Fe-gallate and Mg-gallate MOFs were synthesized rapidly and solvent-free *via* mechanochemistry using a horizontal vibratory ball mill at 30 Hz, underscoring the environmental benefits of this sustainable route. This method drastically reduced reaction times—from hours reported for conventional syntheses to minutes—yielding Fe-gallate in 15 minutes and Mg-gallate in 30 minutes, with both materials reaching stable morphology after 60 minutes. Although isostructural, the MOFs displayed distinct unit cell parameters, pore cavities, and surface areas: Fe-gallate exhibited smaller pores, whereas Mg-gallate presented larger cavities and two protonated oxygen atoms that created acidic sites. Both MOFs can be used for Cr(VI) removal, although they operate through different mechanisms. Fe-gallate exhibits superior performance, achieving a removal efficiency of 29% when applied to a 100 mg L^{-1} Cr solution, and maintaining a relatively stable adsorption capacity over two to three reuse cycles. In contrast, Mg-gallate shows significantly lower adsorption performance, with only 3% Cr removal. This limited efficiency is attributed to chemical reactions likely occurring at its acidic sites, which promote structural degradation and result in the release of Mg into the surrounding medium, what also limited the reuse in one cycle. When applied to soils, Fe-gallate MOF consistently reduced chromium concentrations, with the strongest effects in systems with low to moderate initial contamination. Dose effectiveness depended on the initial Cr levels, achieving reductions of up to 65%. These findings

demonstrate that mechanochemically synthesized Fe- and Mg-gallate MOFs are promising materials for Cr remediation, with distinct adsorption behaviours that may be tailored to different environmental contexts.

Conflicts of interest

There are no conflicts to declare.

Data availability

All generated data in this work are included in this article and in the supplementary information (SI). Supplementary information is available. See DOI: https://doi.org/10.1039/d5mr00123d.

Acknowledgements

We gratefully acknowledge support of the RCGI – Research Centre for Gas Innovation, hosted by the University of São Paulo (USP) and sponsored by FAPESP – São Paulo Research Foundation (2014/50279-4 and 2020/15230-5) and Shell Brasil, and the strategic importance of the support given by ANP (Brazil's National Oil, Natural Gas and Biofuels Agency) through the R&D levy regulation. We also acknowledge the financial support received from FAPESP (2021/00675-4 and 2020/14955-6). LMR acknowledges CNPq for the PQ-A fellowship (303510/2025-0).

References

1 R. K. Feller and A. K. Cheetham, *Solid State Sci.*, 2006, **8**, 1121–1125.
2 D. Wang, H. Yao, J. Ye, Y. Gao, H. Cong and B. Yu, *Small*, 2024, **20**, 2404350.
3 I. Imaz, M. Rubio-Martínez, J. An, I. Solé-Font, N. L. Rosi and D. Maspoch, *Chem. Commun.*, 2011, **47**, 7287–7302.
4 U. Shashikumar, S. Joshi, A. Srivastava, P.-C. Tsai, K. D. S. Shree, M. Suresh, B. Ravindran, C. M. Hussain, S. Chawla, L.-Y. Ke and V. K. Ponnusamy, *Int. J. Biol. Macromol.*, 2023, **253**, 127120.
5 J. Wang, L. Li, L. Guo, Y. Zhao, D. Xie, Z. Zhang, Q. Yang, Y. Yang, Z. Bao and Q. Ren, *Chem.–Eur. J.*, 2019, **25**, 15516–15524.
6 J. Chen, J. Wang, L. Guo, L. Li, Q. Yang, Z. Zhang, Y. Yang, Z. Bao and Q. Ren, *ACS Appl. Mater. Interfaces*, 2020, **12**, 9609–9616.
7 D. Marchetti, E. Dalcanale, R. Pinalli, M. Gemmi, A. Pedrini and C. Massera, *RSC Mechanochem.*, 2025, **2**, 662–669.
8 G. Lin, B. Zeng, J. Li, Z. Wang, S. Wang, T. Hu and L. Zhang, *Chem. Eng. J.*, 2023, **460**, 141710.
9 M. Ismail, M. A. Bustam and Y. F. Yeong, *Crystals*, 2020, **10**, 1006.
10 B. Badhani, N. Sharma and R. Kakkar, *RSC Adv.*, 2015, **5**, 27540–27557.
11 S. Dhiman, G. Mukherjee, in *Recent Developments in Microbial Technologies. Environmental and Microbial Biotechnology*, ed. R. Prasad, V. Kumar, J. Singh, C. P. Upadhyaya, Springer, Singapore, 2021, pp. 163–202.
12 F. H. A. Fernandes and H. R. N. Salgado, *Crit. Rev. Anal. Chem.*, 2016, **46**, 257–265.
13 Z. Noraee, A. Jafari, M. Ghaderpoori, B. Kamarehie and A. Ghaderpoury, *J. Environ. Health Sci. Eng.*, 2019, **17**, 701–709.
14 S. K. Springthorpe, C. M. Dundas and B. K. Keitz, *Nat. Commun.*, 2019, **10**, 5212.
15 A. García, B. Rodríguez, M. Rosales, Y. M. Quintero, P. G. Saiz, A. Reizabal, S. Wuttke, L. Celaya-Azcoaga, A. Valverde and R. Fernández de Luis, *Nanomaterials*, 2022, **12**, 4263.
16 U. Zulfiqar, F. U. Haider, M. Ahmad, S. Hussain, M. F. Maqsood, M. Ishfaq, B. Shahzad, M. M. Waqas, B. Ali, M. N. Tayyab, S. A. Ahmad, I. Khan and S. M. Eldin, *Front. Plant Sci.*, 2022, **13**, DOI: 10.3389/fpls.2022.1081624.
17 O. Christiana Folorunso, *World J. Adv. Res. Rev.*, 2022, **16**, 1358–1370.
18 P. J. Saines, H. H.-M. Yeung, J. R. Hester, A. R. Lennie and A. K. Cheetham, *Dalton Trans.*, 2011, **40**, 6401–6410.
19 N. Heymans, S. Bourrelly, P. Normand, E. Bloch, H. Mkhadder, L. Cooper, M. Gorman, I. Bouzidi, N. Guillou, G. De Weireld and T. Devic, *J. Phys. Chem. C*, 2020, **124**, 3188–3195.
20 M. Sharma and P. Kumar, *Inorg. Chem. Commun.*, 2025, **171**, 113590.
21 B. Azhar, A. E. Angkawijaya, S. P. Santoso, C. Gunarto, A. Ayucitra, A. W. Go, P. L. Tran-Nguyen, S. Ismadji and Y.-H. Ju, *Sci. Rep.*, 2020, **10**, 19212.
22 P. Singh, H. D. Singh, R. Vysyaraju, G. Liske, P. Shekhar, Y. K. Singh, A. Rajendran and R. Vaidhyanathan, *Chem. Mater.*, 2025, **37**, 5476–5486.
23 S. Kumar, S. Jain, M. Nehra, N. Dilbaghi, G. Marrazza and K.-H. Kim, *Coord. Chem. Rev.*, 2020, **420**, 213407.
24 T. Stolar and K. Užarević, *CrystEngComm*, 2020, **22**, 4511–4525.
25 L. Sondermann, Q. Smith, T. Strothmann, A. Vollrath, T. H. Yen Beglau and C. Janiak, *RSC Mechanochem.*, 2024, **1**, 296–307.
26 Q. Chen, Z.-W. Li, S. Huang, G. Chen and G. Ouyang, *RSC Mechanochem.*, 2025, **2**, 336–350.
27 A. Pichon, A. Lazuen-Garay and S. L. James, *CrystEngComm*, 2006, **8**, 211–214.
28 A. Sala, M. D. Faye Diouf, D. Marchetti, L. Pasquale and M. Gemmi, *Cryst. Growth Des.*, 2024, **24**, 3246–3255.
29 J. Beamish-Cook, K. Shankland, C. A. Murray and P. Vaqueiro, *Cryst. Growth Des.*, 2021, **21**, 3047–3055.
30 D. Yuan, C. Shang, J. Cui, W. Zhang and Y. Kou, *Environ. Res.*, 2023, **216**, 114616.
31 H. Niu, Y. Zheng, S. Wang, S. He and Y. Cai, *J. Mater. Chem. A*, 2017, **5**, 16600–16604.
32 C. Lian, J. Liu, W. Wei, X. Wu, T. Goto, H. Li, R. Tu and H. Dai, *Bioact. Mater.*, 2024, **38**, 181–194.
33 Z. Bao, J. Wang, Z. Zhang, H. Xing, Q. Yang, Y. Yang, H. Wu, R. Krishna, W. Zhou, B. Chen and Q. Ren, *Angew. Chem.*, 2018, **130**, 16252–16257.
34 A. Ponce, L. B. Brostoff, S. K. Gibbons, P. Zavalij, C. Viragh, J. Hooper, S. Alnemrat, K. J. Gaskell and B. Eichhorn, *Anal. Chem.*, 2016, **88**, 5152–5158.

35 O. F. Jafter, S. Lee, J. Park, C. Cabanetos and D. Lungerich, *Angew. Chem., Int. Ed.*, 2024, **63**, e202409731.
36 H. M. Younis, A. O. Youssef, S. M. El-Sheikh, S. M. Sheta and M. S. Attia, *Microchem. J.*, 2023, **194**, 109297.
37 C.-H. Wunderlich, R. Weber and G. Bergerhoff, *Z. Anorg. Allg. Chem.*, 1991, **598**, 371–376.
38 A. Corma and H. García, *Chem. Rev.*, 2002, **102**, 3837–3892.
39 L. Cooper, T. Hidalgo, M. Gorman, T. Lozano-Fernández, R. Simón-Vázquez, C. Olivier, N. Guillou, C. Serre, C. Martineau, F. Taulelle, D. Damasceno-Borges, G. Maurin, Á. González-Fernández, P. Horcajada and T. Devic, *Chem. Commun.*, 2015, **51**, 5848–5851.
40 J. Fonseca, L. Meng, I. Imaz and D. Maspoch, *Chem. Soc. Rev.*, 2023, **52**, 2528–2543.
41 S. Singh, N. Sivaram, B. Nath, N. A. Khan, J. Singh and P. C. Ramamurthy, *npj Clean Water*, 2024, **7**, 124.
42 A. Espina, M. V. Cañamares, Z. Jurašeková and S. Sanchez-Cortes, *ACS Omega*, 2022, **7**, 27937–27949.
43 R. J. Díaz Hidalgo, R. Córdoba, P. Nabais, V. Silva, M. J. Melo, F. Pina, N. Teixeira and V. Freitas, *Heritage Sci.*, 2018, **6**, 63.
44 A. V. Sokolov, Y. A. Morkhova, M. N. Kachalkin and A. A. Shindrov, *New J. Chem.*, 2025, **49**, 12174–12181.
45 P. Hermanková, M. Hermanek and R. Zbořil, *Eur. J. Inorg. Chem.*, 2010, **1110**, 1110–1118.
46 C. Tejada-Tovar, Á. Villabona-Ortiz and R. Ortega-Toro, *J. Compos. Sci.*, 2025, **9**, 36.
47 J. D. Ramsey, L. Xia, M. W. Kendig and R. L. McCreery, *Corros. Sci.*, 2001, **43**, 1557–1572.
48 C. Karthik, V. Sri Ramkumar, A. Pugazhendhi, K. Gopalakrishnan and P. Indra Arulselvi, *J. Taiwan Inst. Chem. Eng.*, 2017, **70**, 282–290.
49 T. Yamashita and P. Hayes, *Appl. Surf. Sci.*, 2008, **254**, 2441–2449.
50 J. E. F. S. Rodrigues, W. S. Rosa, M. M. Ferrer, T. R. Cunha, M. J. Moreno Zapata, J. R. Sambrano, J. L. Martínez, P. S. Pizani, J. A. Alonso, A. C. Hernandes and R. V. Gonçalves, *J. Alloys Compd.*, 2019, **799**, 563–572.